Vortex Pair in ground vicinity : Optimal Perturbation and Optimal Control.

A. WAKIM[a], L. JACQUIN[a],V. BRION[a], A. DOLFI-BOUTEYRE[a]

a. ONERA, DAAA, The French Aerospace Lab, 92190 Meudon, France
arnold.wakim@onera.fr

Abstract :

The risk of wake vortex encounter is a major issue in aviation. This is notably true in the vicinity of airports during take-off and landing. In order to reduce wake vortex encounters, conservative separation distances are applied. However, these distances impede on the increase of the frequency of arrivals and departures at airports by the steadily increasing traffic.
In the present work, an analysis of the control of the two-dimensional vortex dynamics close and at the ground as a mean to reduce the separation distance is carried out. The behavior of vortices in ground effect has been a much investigated subject, motivated by this aviation issue but also by wall bounded turbulence (Stephan et al. 2013). It has been demonstrated that vortices (Harvey et al. 1971) rebound at the ground instead of going sideways like in the inviscid situation (Lamb 1932). Vortex rebound causes vortices to stay longer above runways and increase the risk of encounters.
Two control strategies are described in order to alleviate the aforementioned issue. The first one is based on an optimal perturbation approach aiming at mitigating vortices by increasing perturbations growth. An analysis of the effect of the perturbation symmetry and horizon time, along with a physical mechanism of the transient growth processes is achieved. The second approach is based on the optimal control of the vortex position through the implementation of active blowing/suction at the ground. The maximization of the lateral position of the vortices is achieved with the idea of suppressing vortex rebound, and promoting an inviscid like kinematics of the vortices (the vortices move sideways out of the runway). The method achieves a 50% increase in the lateral position of the vortices. A physical analysis of the change induced by the control on the flow is detailed.

Key words : Vortex wall interactions, optimal perturbations, optimal control, constrained optimization

1 Introduction

The increase of air traffic and super jumbo aircrafts pose important issues as regards to wake vortices. Take-off and landing phases are particularly critical due to the proximity of the ground and the fact that encountering trailing vortices can induce a loss of lift. Air traffic is currently ruled by the ATC (Air Traffic Control) procedure, established by the ICAO in the 70's. The ICAO classified aicrafts in three main categories (light, medium and heavy) and two additional for the A380 and the B747. In the case of a heavy aircraft landing after an Airbus A380, current impose a separation distance of eight nautical

miles which corresponds to approximately a three minute latency. Solutions to hasten vortex decay at the ground could increase airport capacity and traffic security at the same time.
The dynamics of counter-rotating vortex pairs in ground effect has been studied intensively over the past century. For an inviscid fluid, the centroids trajectories are hyperbolae branches of the form $\frac{1}{x^2}+\frac{1}{y^2}=\frac{1}{x_0^2}+\frac{1}{y_0^2}$ (Sir Horace Lamb [3]). In this situation, vortices escape the trajectory of the following aircrafts and rapidly become harmless. There is a substantial body of literature concerning aircraft trailing vortices in ground effect (see Donaldson and Bilanin [4] for instance). The effect of viscosity causes the rebound of trailing vortices as they approach the ground. Dee and Nicholas [5] first observed this phenomenon in an experimental study of smoke-marked aircraft vortices in ground effect. This effect has been conjectured by Harvey and Perry [2] in 1971 using a moving floor technique in a wind tunnel. Multiple theoretical and numerical models have subsequently been employed to study vortex-ground interactions. Peace and Riley [6], Orlandi [7] have used a Navier-Stokes based approach. Zheng [8] et al. and Türk et al. [9] used a vorticity-stream function computational model in order to increase the Reynolds over a wide range (up to $Re = 3.10^6$), however it does not consider turbulence effects.

This work is dedicated to enhance the decay of vortices decay near the ground. One approach is by employing optimal perturbations that maximize the kinetic energy of the perturbations for a given time horizon. Such perturbations may accelerate transition to turbulence and thus shorten the lifetime of vortices above runways. We use a direct-adjoint technique of constrained optimization in which the initial perturbation velocity field maximizes a chosen objective function (e.g. kinetic energy). The constraints are the linarized Navier-Stokes equations for the perturbation.

Another way to shorten the presence of a vortex is based on optimal control. Also based on a direct-adjoint strategy, this method aims at maximizing the absolute value of the lateral position of the vortices by using an appropriate blowing/sucking strategy at the ground. This would not accelerate decay but evacuate vortices from the runway much quicker, in a manner identical to the inviscid case.

The remainder of this paper is organized as follows. In §2 we define the governing equations describing the dynamics of wake vortices in ground effect, while in §3 we briefly introduce the numerical setup. In §4, we present the mechanism leading to energy growth through the use of optimal perturbations. Finally in §5 we detail the optimal control method applied on maximizing the lateral position of vortices.

2 Vortices in ground effect

In the following, the fluid domain is the upper half plane (x, y) such that $y = 0$ denotes the ground. The base flow is initialized by superimposition of a pair of counter-rotating Lamb-Oseen vortices with a circulation Γ, a vortex separation b and a core radius a. We non-dimensionalize lengths with the vortex separation b and the velocities with the drift velocity of the vortex pair $v_{drift} = \frac{\Gamma}{2\pi b}$. The time is hence normalized on the time of descent of a vortex pair $T_{drift} = \frac{2\pi b^2}{\Gamma}$. Unless otherwise stated all the quantities will be dimensionless from this point forward. We define the circulation-based Reynolds number as $Re = \frac{\Gamma}{2\pi\nu}$. The governing equations for the base flow are the following :

$$\begin{gathered}\partial_t \boldsymbol{U} + \boldsymbol{U}\cdot\boldsymbol{\nabla}\boldsymbol{U} + \boldsymbol{\nabla}P - \frac{1}{Re}\boldsymbol{\nabla}^2\boldsymbol{U} = 0 \\ \boldsymbol{\nabla}\cdot\boldsymbol{U} = 0 \\ \boldsymbol{U}(x,0,t) = 0 \ ; \ \boldsymbol{U}(\pm\infty,+\infty,t) = 0\end{gathered} \tag{1}$$

We display in figure (1), snapshots of the vorticity distribution, for different instants. Initially the vortex pair is located in $(x_0, y_0) = (\pm 0.5, 2.0)$, corresponding to the inviscid trajectory with $(x_\infty, y_\infty) = (\pm 0.5, +\infty)$. As the vortex pair descends, a boundary layer grows (1a) in which an intense pressure gradient occurs that brings the detachment of the boundary layer (1b). The separation produces secondary vortices of opposite vorticity whose strengths increase rapidly, hence causing the upward motion of the primary vortex (1c).

(a) Growing boundary layer as the vortex pair approaches the ground.

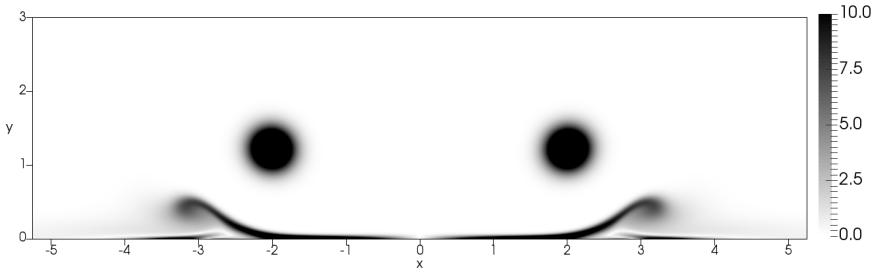

(b) Separation of the vorticity sheets due to the adverse pressure gradient.

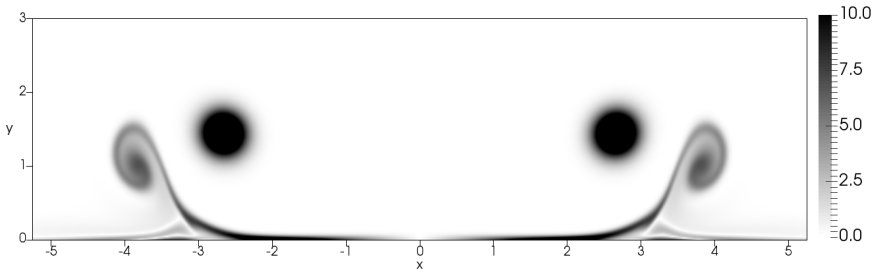

(c) Formation of the secondary vortices which cause the primary ones to ascend.

FIGURE 1 – Snapshots of the evolution of the vorticity magnitude of a counter-rotating vortex pair in ground effect showing the rebound phenomenon after separation of the boundary layer. Simulation carried out for $Re = 1200$.

The secondary vortices orbit around the primary ones, which gives rise to the *rebound phenomenon* as

vorticity sheets detach successively from the boundary layers. This phenomenon may occur multiple times (see [9]) therefore causing the vortices to remain longer above the runways, see figure (2).

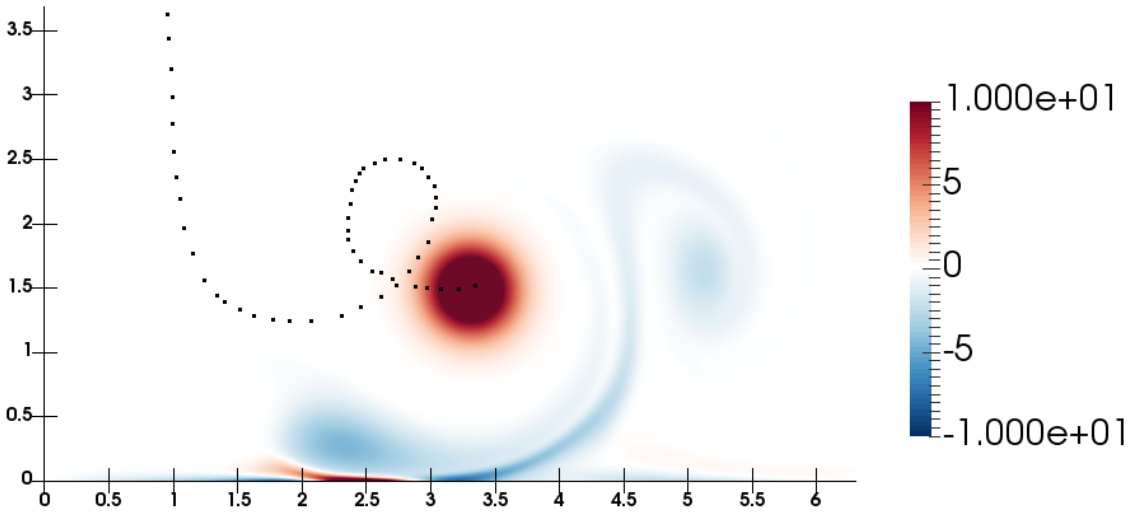

FIGURE 2 – Vorticity field showing the evolution of the centroid trajectory (black dots) initially located in $(x_0, y_0) = (1, 3.8)$. For clarity, only the right vortex of the pair, $x > 0$ is displayed. The vortex is subject to rebounds as the boundary layer separates provoking the looping of the centroid. This phenomenon occurs multiple times.

3 Numerical Setup

Nek5000, a spectral element solver for the incompressible Navier-Stokes equations [13], is used for the simulations. To validate the computations, the results presented in earlier studies are reproduced using Nek5000 in figure (3). It compares the vortex trajectories obtained by Türk et al. [9] and Zheng et al. [11] with the ones computed with Nek5000.

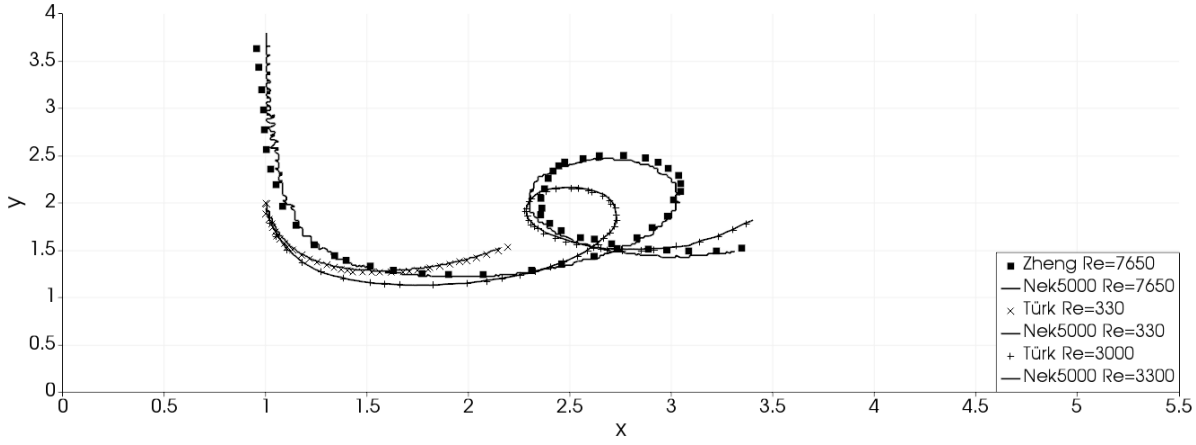

FIGURE 3 – Comparison of the centroid trajectories obtained by Zheng [11] and Türk [9] with the ones obtained using Nek5000, for $Re = 330$, 3300 and 7650.

The computations are carried out in a rectangular domain of size $20b \times 10b$. A convergence strudy has been achieved to validate the simulation. No-slip boundary condition is prescribed at the ground. On the

other boundaries, symmetry boundary conditions are applied. The trajectories computed via Nek5000 are found to be in good agreement with the earlier results.

4 Optimal Perturbations

In this section, we aim to study optimal perturbations. The initial condition that leads to the largest perturbation growth over a given period of time T, is calculated. The non-normality of the Navier-Stokes operator leads to a non-orthogonal set of eigenvectors. The superimposition of such eigenvectors may lead to algebraic perturbation growth.

4.1 Variational Approach

The governing equations are the two-dimensional linearized Navier-Stokes equations for the perturbations :

$$\begin{aligned} \partial_t \boldsymbol{u'} + \boldsymbol{U}\cdot\boldsymbol{\nabla}\boldsymbol{u'} + \boldsymbol{u'}\cdot\boldsymbol{\nabla}\boldsymbol{U} + \boldsymbol{\nabla}p - \frac{1}{Re}\boldsymbol{\nabla}^2\boldsymbol{u'} = 0 \\ \boldsymbol{\nabla}\cdot\boldsymbol{u'} = 0 \end{aligned} \tag{2}$$

where $(\boldsymbol{u'}, p)$ describe the perturbation velocity field and pressure, and $Re = \dfrac{\Gamma}{2\pi\nu}$. The initial field is denoted $\boldsymbol{u'_0}$. The goal is to maximize the kinetic energy of the perturbations over a chosen time horion T, hence the cost functional of interest is given by :

$$\mathcal{J}(\boldsymbol{u'}, \boldsymbol{u'_0}, T) = \frac{E(\boldsymbol{u'}(T))}{E(\boldsymbol{u'_0})} \tag{3}$$

where $E(\boldsymbol{u'}(T)) = \dfrac{1}{2}\displaystyle\int_V \boldsymbol{u'}^2(x, y, T)$ denotes the kinetic energy at $t = T$. Note that we choose to normalize $\boldsymbol{u'_0}$ such that its kinetic energy equals unity, due to the linearity of equation (2). This problem is solved using Lagrange multipliers technique introducing *adjoint variables* denoted $(\tilde{u}, \tilde{p})$. The constraints are added to the cost functional form the Lagrangian :

$$\begin{aligned} \mathcal{L}(\boldsymbol{u'}, p, \boldsymbol{u'_0}, \tilde{\boldsymbol{u'}}, \tilde{p}, \tilde{\boldsymbol{u'_0}}) = \mathcal{J}(\boldsymbol{u'}, \boldsymbol{u'_0}) - \left\langle \tilde{\boldsymbol{u'}}\,, \partial_t \boldsymbol{u'} + \boldsymbol{U}\cdot\boldsymbol{\nabla}\boldsymbol{u'} + \boldsymbol{u'}\cdot\boldsymbol{\nabla}\boldsymbol{U} + \boldsymbol{\nabla}p - \frac{1}{Re}\boldsymbol{\nabla}^2\boldsymbol{u'} \right\rangle \\ - \left\langle \tilde{p}, \boldsymbol{\nabla}\cdot\boldsymbol{u'} \right\rangle - \left[\tilde{\boldsymbol{u'_0}}, \boldsymbol{u'_0} - \boldsymbol{u'}(0) \right] \end{aligned} \tag{4}$$

where $\langle\cdot,\cdot\rangle$ and $[\cdot,\cdot]$ represent the following inner products :

$$\begin{aligned} \langle a, b\rangle &= \int_0^T \int_V a(x, y, t) b(x, y, t)\ \mathrm{d}V\ \mathrm{d}t \\ [c, d] &= \int_V c(x, y) d(x, y)\ \mathrm{d}V \end{aligned} \tag{5}$$

The optimal perturbation is obtained by equating the first variation of the Lagrangian to zero. The variation of $\mathcal{L}$ with respect to the direct variables, $(\boldsymbol{u'}, p, \boldsymbol{u'_0})$, yields a set of equation governing the adjoint

variables $(\tilde{\boldsymbol{u'}}, \tilde{p}, \tilde{\boldsymbol{u'_0}})$:

$$\begin{gathered} -\partial_t \tilde{\boldsymbol{u'}} - \boldsymbol{U} \cdot \boldsymbol{\nabla} \tilde{\boldsymbol{u'}} + \tilde{\boldsymbol{u'}} (\cdot \boldsymbol{\nabla} \boldsymbol{U})^\intercal - \boldsymbol{\nabla} \tilde{p} - \frac{1}{Re} \boldsymbol{\nabla}^2 \tilde{\boldsymbol{u'}} = 0 \\ \boldsymbol{\nabla} \cdot \tilde{\boldsymbol{u'}} = 0 \end{gathered} \tag{6}$$

As a consequence of the minus sign in front of the time derivative term in equation (6), the adjoint equation is solved from $t = T$ to $t = 0$. Then one finds the initialization of the adjoint $\tilde{\boldsymbol{u'}}(x, y, T)$ by taking the first variation of the Lagrangian with respect to $\boldsymbol{u'}(x, y, T)$ and matching the results coming from the integration by part. One finds

$$\tilde{\boldsymbol{u'}}(T) = \frac{\boldsymbol{u'}(x, y, T)}{E(\boldsymbol{u'_0})} \tag{7}$$

and the gradient of the Lagrangian with respect to the initial condition is :

$$\boldsymbol{\nabla}_{\boldsymbol{u'_0}} \mathcal{L} = \boldsymbol{\nabla}_{\boldsymbol{u'_0}} \mathcal{J} - \tilde{\boldsymbol{u'_0}} \tag{8}$$

A rotation based algorithm respecting the unit-norm constraint is used, see Douglas [14]. The overall optimization process goes as :

1. Choice of the initial guess : symmetric or anti-symmetric random white noise.
2. Normalization of the kinetic energy $E(\boldsymbol{u'}_{\boldsymbol{0},n}) = 1$
3. Time integration of the governing equations (2) from $t = 0$ to $t = T$, evaluation of $\mathcal{J}_n(\boldsymbol{u'}, \boldsymbol{u'_0})$
   (a) If $\mathcal{J}_n(\boldsymbol{u'}, \boldsymbol{u'_0}) > \mathcal{J}_{n-1}(\boldsymbol{u'}, \boldsymbol{u'_0})$ then go to 4
   (b) Else : go to 5b
4. Adjoint solving from $t = T$ to $t = 0$.
5. Update based on the rotation method [14]
   (a) If $\mathcal{J}_n(\boldsymbol{u'}, \boldsymbol{u'_0}) > \mathcal{J}_{n-1}(\boldsymbol{u'}, \boldsymbol{u'_0})$ then $\boldsymbol{u'}_{\boldsymbol{0},n+1} = \boldsymbol{u'}_{\boldsymbol{0},n} cos(\alpha) + \boldsymbol{G}_n \sin(\alpha)$ (where $\boldsymbol{G}_n$ is the projection of $\boldsymbol{\nabla}_{\boldsymbol{u'}_{\boldsymbol{0},n}} \mathcal{J}$ on a plane perpendicular to $\boldsymbol{u'}_{\boldsymbol{0},n}$)
   and $\alpha \longrightarrow \alpha$
   (b) Else $\alpha \longrightarrow \dfrac{\alpha}{2}$
6. Go to 2.

4.2 Results

In this section we demonstrate that significant gain in kinetic energy is achieved and that the nature of the perturbations and the time horizon T play a major role on the structure of the optimal perturbation. The baseflow being symmetric with respect to $x = 0$, two orthogonal subsets of perturbations can be considered : symmetric and anti-symmetric. Symmetric perturbations are the one that verify mirror symmetry with respect to $x = 0$, that is :

$$\begin{aligned} u'(-x, y, t) &= -u'(x, y, t) \\ v'(-x, y, t) &= v'(x, y, t) \end{aligned}$$

These perturbations are denoted by *SYM*. On the other hand, anti-symmetric perturbations verify anti-symmetry with respect to $x = 0$,

$$\begin{aligned} u'(-x, y, t) &= u'(x, y, t) \\ v'(-x, y, t) &= -v'(x, y, t) \end{aligned} \tag{9}$$

These perturbations are denoted by *ASYM*. The simulations are carried out for $Re = 100$ and $T \in [0; 5]$.

The growth of the kinetic energy of the perturbations is described by Reynolds-Orr equation (10) (see [15]).

$$\mathrm{d}_t E = -\int_V \boldsymbol{u'}^{\mathsf{T}} \cdot \underline{\underline{\boldsymbol{\nabla} \boldsymbol{U}}} \cdot \boldsymbol{u'} \, \mathrm{d}V - \frac{1}{Re} \int_V \boldsymbol{\nabla} \boldsymbol{u'} : \boldsymbol{\nabla} \boldsymbol{u'} \, \mathrm{d}V \tag{10}$$

The first term on the right hand side of equation (10) corresponds to production of kinetic energy by the alignment of the perturbations with the directions of strain rate tensor of the base flow and the second term represents viscous dissipation. As is evident from the equation, the flow region where the shear production per unit volume is negative contributes to the growth of the perturbations. Only the strain rate tensor participates in the growth of the perturbations. When the perturbations are aligned with the eigenvector associated to the negative eigenvalue of the strain rate, the kinetic energy increases. Figure (4) shows the negative eigenvalue of the strain rate tensor.

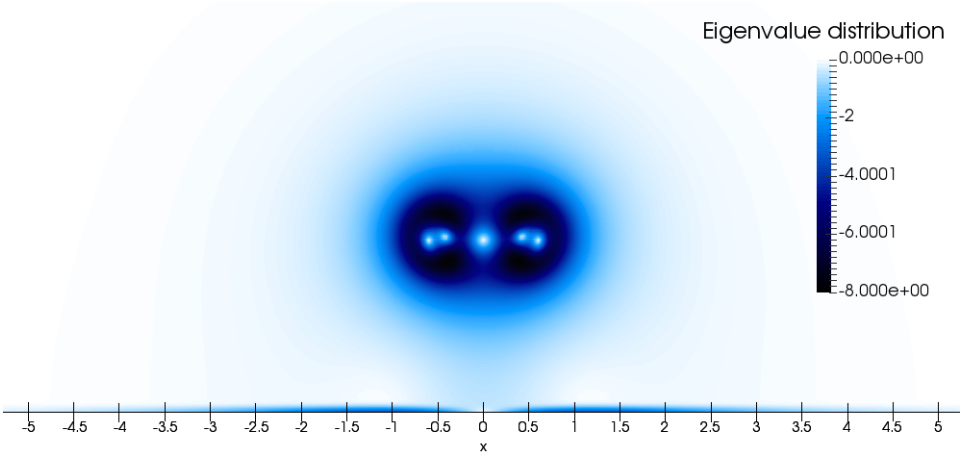

FIGURE 4 – Distribution of the negative eigenvalue of the strain rate tensor

Figure (5) shows the vorticity distribution of the optimal perturbation computed for $T = 1.5$ and $T = 4$. The base flow streamlines, computed in the reference frame moving with the counter-rotating vortices, are represented in black lines.

Initially, the optimal perturbations are principally located in the Kelvin oval of the base flow, on the symmetry axis $x = 0$ and near the ground. Figure (6) shows the downwards motion of the perturbation due to the advection of the base flow and the appearance of a *displacement mode* (see [16]).

As time increases the boundary layer induced by the perturbation, separates and detaches from the ground forming lobes of vorticity around the displacement mode. as shown in figure (7)

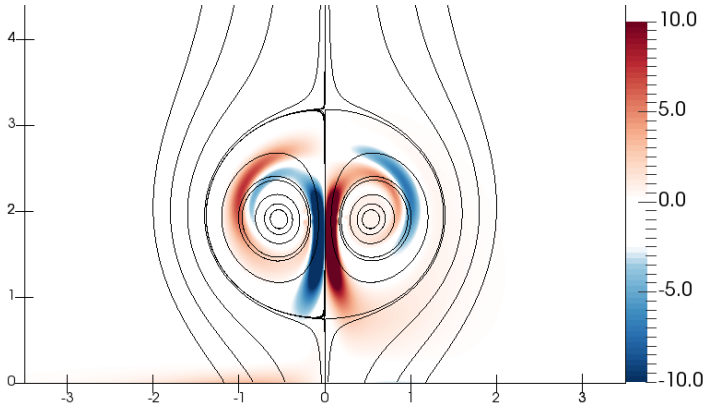

(a) Vorticity distribution of the symmetric optimal perturbation computed for $T = 1.5$

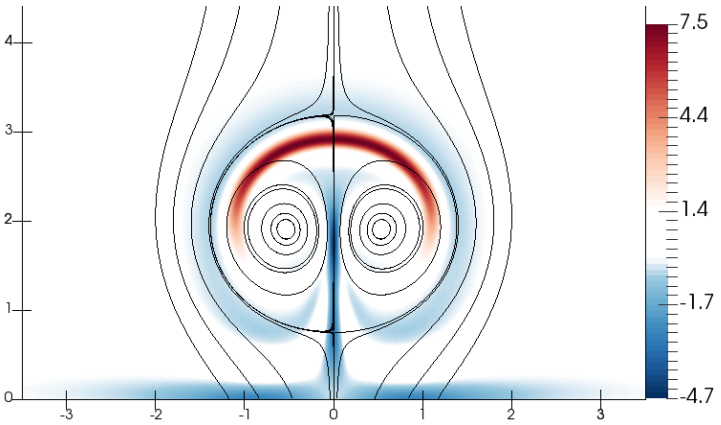

(b) Vorticity distribution of the anti-symmetric optimal perturbation computed for $T = 4$

FIGURE 5 – Vorticity distribution at $t = 0$ of the optimal perturbation computed for the symmetric optimal perturbation a) $T = 1.5$ and the anti-symmetric optimal perturbation b) $T = 4$

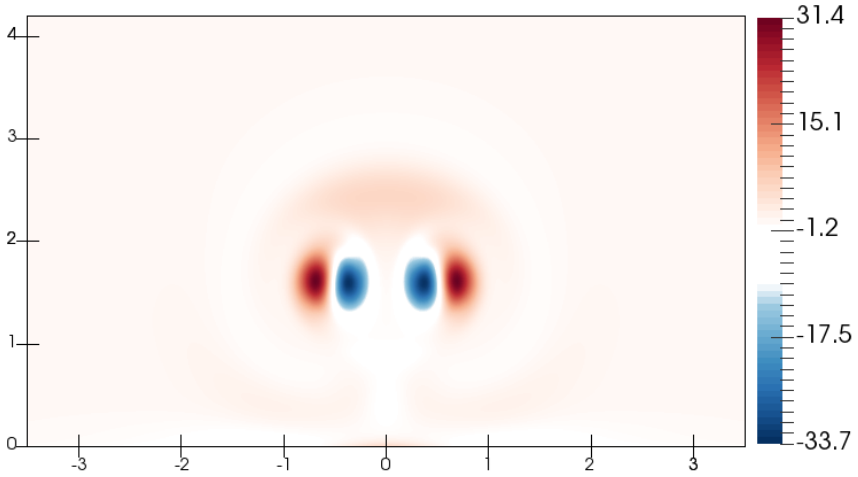

FIGURE 6 – Vorticity distribution at $t = \dfrac{T}{10} = 0.4$ of the anti-symmetric optimal perturbation showing the displacement mode.

In figure (8) we plot the values of the cost functional $\mathcal{J}(\boldsymbol{u'}, \boldsymbol{u'_0}, T)$ as a function of T for symmetric and anti-symmetric optimal perturbation. The cost functional increases and then decreased for higher values

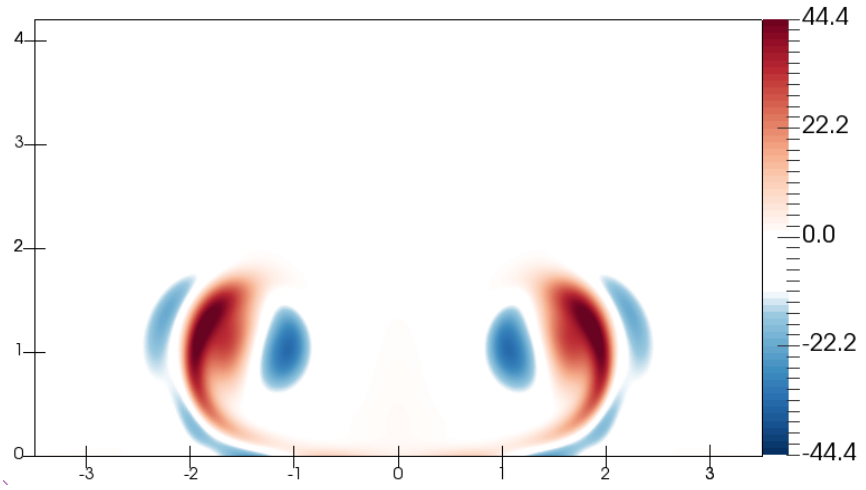

FIGURE 7 – Vorticity distribution at $t = T = 4$ of the anti-symmetric optimal perturbation.

of the horizon time.

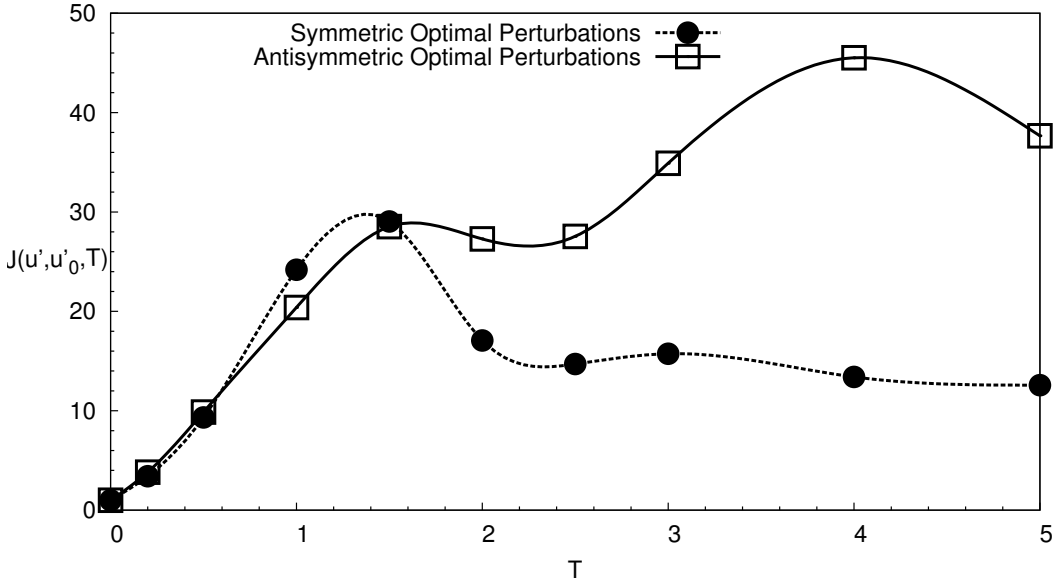

FIGURE 8 – Gain in energy as a function of the time horizon T for symmetric and anti-symmetric perturbations showing the dependency of time horizon on the symmetrty of the optimal perturbation. For all T except $T \in [0.5; 1]$ optimal perturbations are anti-symmetric. Marked points have been computed, the interpolating curves have been computed using cubic splines.

5 Optimal control

In this part an optimal control strategy applicable to the full flow field is undertaken. An optimal forcing at the ground is sought in order to reduce the wake issue. A starting point is the equation for the enstrophy

$$\frac{\mathrm{d}\mathcal{E}}{\mathrm{d}t} = \frac{1}{Re}\oint_{\partial V} \omega(\boldsymbol{\nabla}\omega \cdot \boldsymbol{n})\mathrm{d}\Gamma - \frac{1}{Re}\int_V |\boldsymbol{\nabla}\omega|^2 \,\mathrm{d}V \tag{11}$$

following which it can be understood that a reduction in the intensity of the wake vortices can be obtained either by acting at the frontier of the flow field (first term in the RHS) or by increasing viscous diffusion (second term in the RHS). In the current laminar setting and with a given vortex structure, there no possibility to increase enstrophy diffusion. However by acting at the wall it seems possible to drive the dynamics of the vorticity. Koumoutsakos [21] applied active control of the vorticity flux at the wall in order to enhance vortex decay in the context of wall bounded turbulence. The objective that is applied is here is a maximisation of the lateral position of the vortices at a given horizon time T. Such a control should promote an inviscid like kinematics by suppressing the vortex rebounds. In terms of application, this is of direct interest as the vortices would move away from the runways.

Unlike in the previous section, the total flow field $\boldsymbol{u}$ is considerd, with the governing equations

$$\begin{gathered} \partial_t \boldsymbol{u} + \boldsymbol{u}\cdot\boldsymbol{\nabla}\boldsymbol{u} + \boldsymbol{\nabla}P - \frac{1}{Re}\boldsymbol{\nabla}^2\boldsymbol{u} = 0 \\ \boldsymbol{\nabla}\cdot\boldsymbol{u} = 0 \\ u(x, y=0, t) = u_w(x,t) \;\;,\;\; v(x, y=0, t) = v_w(x,t) \end{gathered} \tag{12}$$

where the subscript $\cdot_w$ stands for "wall". As previously, the flow field is initialized with a pair of counter-rotating Lamb-Oseen vortices with $(x_0, y_0) = (\pm 0.5, 2.5)$. Due to the flow symmetry only the right half of the domain is considered $x \geq 0$.

5.1 Theoretical Framework

Equation 11 describes the evolution of enstrophy, $\mathcal{E}$, for wall bounded flows.

The objective functional writes

$$\mathcal{K}(\boldsymbol{u}, \boldsymbol{u}_w, T) = \frac{\int_V x\,\omega^2(x,y,T)\mathrm{d}V}{\int_V \omega^2(x,y,T)\mathrm{d}V} - \frac{l^2}{2}\int_0^T \int_{\Gamma_{wall}} u_w^2(x,t) + v_w^2(x,t)\,\mathrm{d}x\mathrm{d}t \tag{13}$$

where ω denotes the z-component of the vorticity. The first integral represents the barycenter of the square of the vorticity. It allows to maximize the lateral position of all vortical structures present in the flow. The second term is the cost of the forcing which makes the problem mathematically convex. The tuning parameter l prevents the control from being arbitrarily large. Ultimately the control is applied on a limited portion of the ground, $x \leq 15b$.

The constrained optimization problem is solved with the Lagrange multipliers method. The adjoint variables are described by $(\tilde{\boldsymbol{u}}, \tilde{p}, \tilde{\boldsymbol{u}}_w)$. The Lagrangian function is similar to (4) apart from the term constraining the boundary conditions

$$\begin{aligned}\mathcal{L}(\boldsymbol{u},p,\boldsymbol{u}_0,\boldsymbol{u}_w,\tilde{\boldsymbol{u}},\tilde{p},\tilde{\boldsymbol{u}}_0,\tilde{\boldsymbol{u}}_w) = \mathcal{K}(\boldsymbol{u},\boldsymbol{u}_w) - \left\langle \tilde{\boldsymbol{u}}\ , \partial_t\boldsymbol{u} + \boldsymbol{u}\cdot\boldsymbol{\nabla}\boldsymbol{u} + \boldsymbol{\nabla}p - \frac{1}{Re}\boldsymbol{\nabla}^2\boldsymbol{u'}\right\rangle \\ - \langle\tilde{p},\boldsymbol{\nabla}\cdot\boldsymbol{u}\rangle - [\tilde{\boldsymbol{u}}_0,\boldsymbol{u}_0-\boldsymbol{u}(0)] - (\tilde{\boldsymbol{u}}_w,\boldsymbol{u}(x,0,t)-\boldsymbol{u}_w)\end{aligned} \tag{14}$$

with $(p,q) = \int_0^T \int_{\Gamma_{wall}} p(x,0,t)q(x,0,t)\,\mathrm{d}x\mathrm{d}t$. The adjoint equations yield

$$\begin{gathered}-\partial_t\tilde{\boldsymbol{u}} - \boldsymbol{u}\cdot\boldsymbol{\nabla}\tilde{\boldsymbol{u}} - \tilde{\boldsymbol{u}}\cdot(\boldsymbol{\nabla}\boldsymbol{u})^\intercal - \boldsymbol{\nabla}\tilde{p} - \frac{1}{Re}\boldsymbol{\nabla}^2\tilde{\boldsymbol{u}} = 0 \\ \boldsymbol{\nabla}\cdot\tilde{\boldsymbol{u}} = 0\end{gathered} \tag{15}$$

Matching the term from the integration by parts give the initialization of the adjoint variable and of the adjoint velocity at the ground, in equation 16 and :

$$\begin{aligned}\tilde{u}(x,y,T) &= \frac{2\partial_y\omega\left(x\int_V\omega^2(x,y,T)\mathrm{d}V - \int_V x\omega^2(x,y,T)\mathrm{d}V\right)}{\left(\int_V\omega^2(x,y,T)\mathrm{d}V\right)^2} \\ \tilde{v}(x,y,T) &= \frac{-2\left(\omega+\partial_x\omega\right)\int_V\omega^2(x,y,T) + 2\partial_x\omega\int_V x\omega^2(x,y,T)\mathrm{d}V}{\left(\int_V\omega^2(x,y,T)\mathrm{d}V\right)^2} \\ \tilde{u}_w(x,t) &= \frac{1}{Re}\frac{\partial\tilde{u}}{\partial x}(x,0,t)\ ,\ \tilde{v}_w(x,t) = \tilde{p}(x,0,t) + \frac{1}{Re}\frac{\partial\tilde{v}}{\partial y}(x,0,t)\end{aligned} \tag{16}$$

A steepest descent algorithm is used to find the optimal control. The algorithm converge after 20 iterations. Several initialization procedures have also been tested (zero initial condition, random sum of harmonic functions), that yield the same result.

5.2 Results

Figure 9 shows the right vortex centroid evolution in the case of uncontrolled and controlled flow.

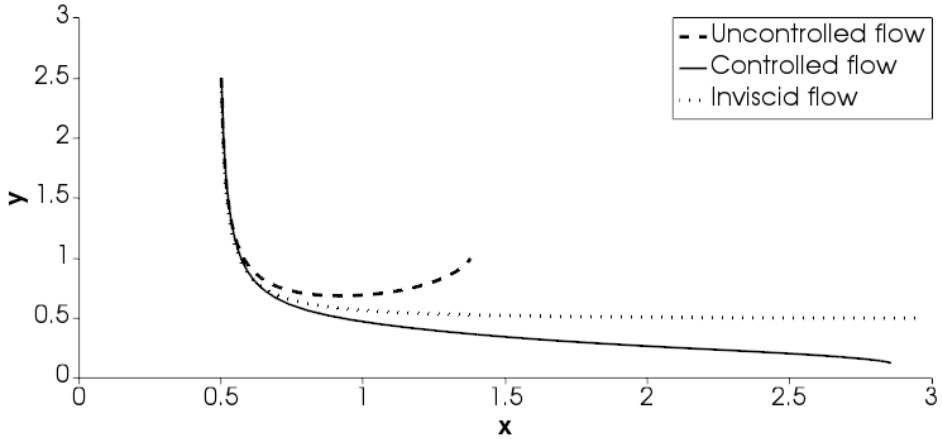

FIGURE 9 – Centroid trajectories in the case of an uncontrolled flow (dashed line), with the optimal control (solid line) and the inviscid flow (dotted line) for $Re = 200$ and $l^2 = 10^{-3}$.

Figure (10) shows the vorticity distribution associated to the points A and B mentioned in figure 9. In A the separation occurs and provokes the detachement of the secondary vortex while in B separation does not occur. Without control the value of the cost functional is about $\mathcal{K}(\boldsymbol{u}, \boldsymbol{u}_w, T) \sim 1.4$. whereas in the case of a controlled flow the optimal value of the cost functional is $\mathcal{K}(\boldsymbol{u}, \boldsymbol{u}_w, T) \sim 3$. The lateral position is more than doubled with control.

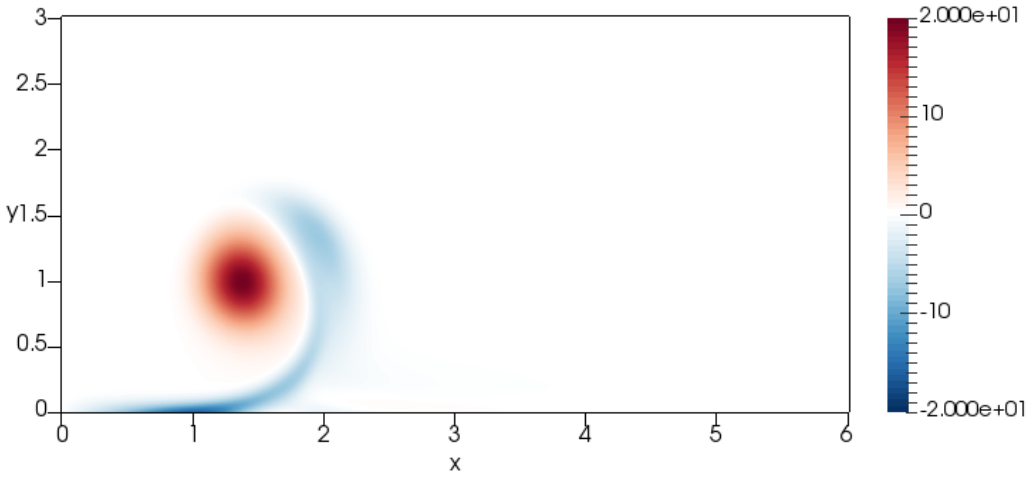

(a) Vorticity distribution of the flow without control at $t = T = 4$. referring to point A in figure 9

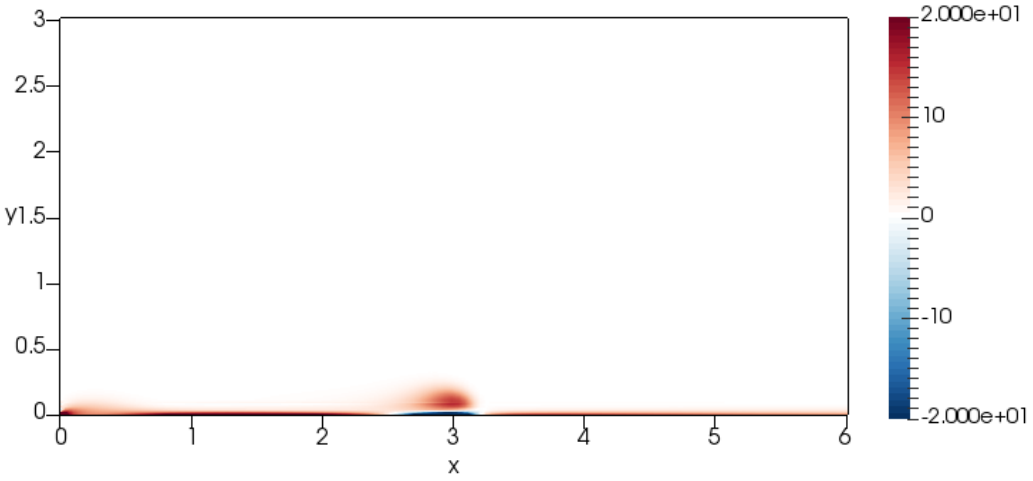

(b) Vorticity distribution of the flow with control at $t = T = 4$. referring to point B in figure 9

FIGURE 10 – Vorticity field at time $t = T$ in the case of the uncontrolled flow (a) and with the optimal at the ground (b). When optimal control is applied, the separation of the boundary layer occuring in (a) is diminished , the rebound does not occur and the lateral position is doubled . Simulation carried out For $Re = 200$ and $l^2 = 10^{-3}$.

Figure (11) shows the control profile as a function of the lateral position for $t = T = 4$. The optimal control velocity components are of the same order of magnitude as the drift velocity of the vortex pair. The horizontal component of the control is always positive while the vertical component changes sign near $x = 0.6$. In the vicinity of the vortex, the fluid is pushed down to the right causing the vortex to move closer to the ground than the inviscid trajectory, see figure 9.

It is interesting to look at the power required by the control. The instantaneous power P per unit length

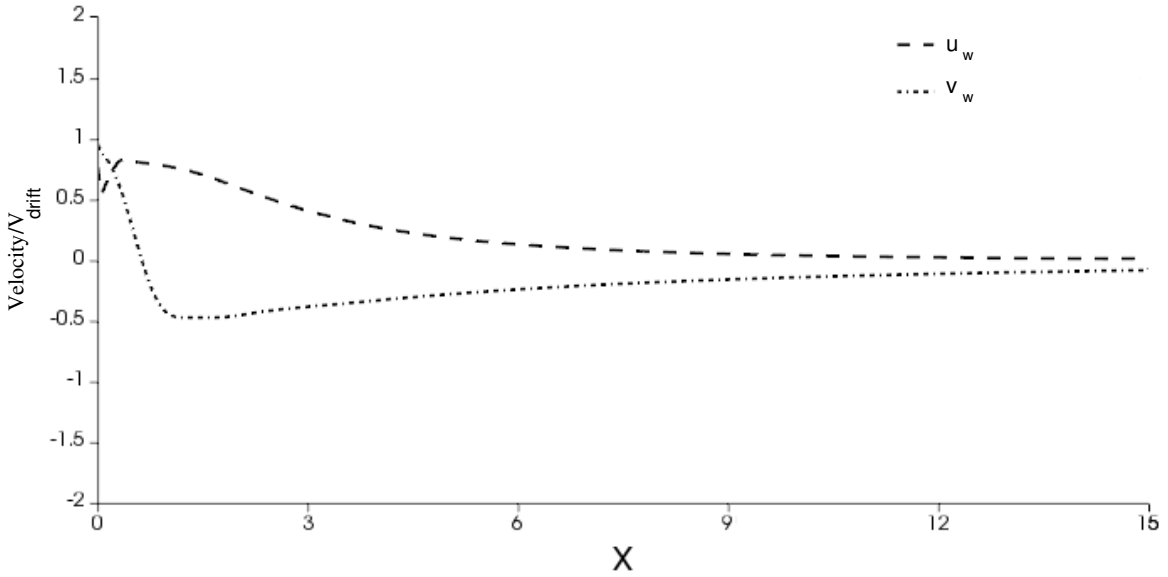

FIGURE 11 – Optimal control velocity profile as a function of x for $Re = 200$ and $l^2 = 10^{-3}$. The dashed line represent $u_w(x,t)$ and the dash-dotted line represent $v_w(x,t)$.

(in the transverse direction) is given by :

$$P = \int_{\partial_{Wall}} |v_w(x,t)| \boldsymbol{u}_w^2(x,t)\, \mathrm{d}x \tag{17}$$

and in physical units

$$P^* = \left(\frac{\Gamma}{2\pi b}\right)^3 b \int_{\partial_{Wall}} |v_w(x,t)| \boldsymbol{u}_w^2(x,t)\, \mathrm{d}x \text{ in } W.m^{-1} \tag{18}$$

Considering an aircraft with $\Gamma = 500m^2.s^{-1}$ and $b = 50m$, the control requires $\sim 10^6 W$ over 50m in the transverse direction.

6 Summary and conclusions

In the present study has applied optimal methods have been applied to increase kinetic energy of the perturbations and promoting inviscid like kinematics of wake vortices in ground effect. It is found that optimal perturbations are located in the Kelvin oval and on the symmetry plane. At $Re = 100$ the influence of the symmetry of the perturbation has been investigated showing the dominance of anti-symmetric perturbations at small horizon time $T < 0.5$ and for larger horizon time $T > 1.5$. Significant gain in kinetic energy is achieved (~ 50) for the linear perturbations due to the appearance of displacement modes.

The optimal control method applied to vortices in ground effect shows encouraging results on maximizing the lateral position of the vortex centroids. Separation of the boundary layer is inhibited hence recovering inviscid like kinematics is obtained. For $Re = 200$ and $T = 4$, the lateral position of the vortices is doubled.

Future work on optimal perturbations will be devoted to studying the influence of the Reynolds number and the dynamics of three-dimensional perturbations.

Concerning optimal control, a parametric study will be carried out to characterize the influence of the Reynolds number and the horizon time on the flow.

Références

[1] Stephan, A., Holzäpfel, F., Misaka, T., 2013, Aircraft wake-vortex decay in ground proximity Physical mechanisms and artificial enhancement, *Journal of Aircraft* Vol. 50, No. 4, p.1250-1260

[2] J.K. Harvey, F.J. Perry, 1971, Flowfield Produced by Trailing Vortices in the Vicinity of the Ground, *The American Institute of Aeronautics Journal*, Vol. 9, No. 8, p. 1659-1660

[3] H. Lamb, 1932, Hydrodynamics, *Cambridge University Press*, No. 6

[4] C.D Donaldson, A.J. Bilanin, 1975, Vortex Wakes of Conventional Aircraft, *AGARDograph*, No. 204

[5] F.W. Dee, O.P. Nicholas, 1968, Flight Measurements of Wing-Tip Vortex Motion near the Ground, *Royal Aeronautical Establishment*, CP-1065

[6] A.J. Peace, N. Riley, 1983, A Viscous Vortex Pair in Ground Effect, *Journal of Fluid Mechanics*, Vol. 129, pp. 409-426

[7] P. Orlandi, 1990, Vortex Dipole Rebound from a Wall, *Physics of Fluids*, Vol. 2, No.8, pp. 1429-1436

[8] Z. C. Zheng, R. L. Ash, 1996, A Study of Aircraft Wake Vortex Behavior Near the Ground, *The American Institute of Aeronautics and Astronautics Journal*, Vol. 34, No.3, pp. 580-589

[9] L. T¸rk, D. Coors, D. Jacob , 1999, Behavior of wake vortices near the ground over a large range of Reynolds numbers, *Institute for Aeronautical and Aerospace Engineering*, No.2, 71-81

[10] R.E. Robins, D.P. Delisi, 1993, Potential Hazard of Aircraft Wake Vortex in Ground Effect with Crosswinds, *Journal of Aircraft*, Vol. 30, No. 2, pp. 201-206

[11] Z. C. Zheng, R. L. Ash, 1993, Prediction of Turbulent Wake Vortex Motion near the Ground, *Transitional and Turbulent Compressible Flows*, Vol. 30, No. 2, pp. 195-207

[12] O. Zeman, 1995, The Persistence of Wake Vortices a Modeling Study, *Physics of Fluids*, Vol.7, No.1, pp. 135-143

[13] P.F. Fischer, J.W. Lottes, S.G Kerkemeier, 2008, Nek5000 web page, http ://nek5000.mcs.anl.gov

[14] Douglas, Scott C., S. Y. Kung, and Shun-ichi Amari, 1998, Gradient adaptation under unit-norm constraints, In Proceedings of the Ninth IEEE SP Workshop on Statistical Signal and Array Processing, pp. 144-147.

[15] Orr, William M.F, 1907, The stability or instability of the steady motions of a perfect liquid and of a viscous liquid. Part I : A perfect liquid., Proceedings of the Royal Irish Academy. Section A : Mathematical and Physical Sciences. Hodges, Figgis, Vol. 27 (1907 - 1909), pp. 9-68

[16] V. Brion, D. Sipp, L. Jacquin, 2014, Linear dynamics of the Lamb-Chaplygin dipole in the two dimensional limit, *Physics of Fluids*, American Institute of Physics, Vol.26, pp.064103.

[17] R. Jugier, L. Joly, P. Brancher, J. Fontane, Instabilités bidimensionnelles d'un dipôle visqueux. (2015), CFM 2015, 24 August 2015 - 28 August 2015 (Lyon, France).

[18] Farell, B. F., 1988, Optimal excitation of perturbations in viscous shear flow. *Physics of Fluids* Vol. 31, pp. 2093-2102.

[19] Hunt, J. C. R., Wray, A.A, Moin, P., 1988, Eddies, Streams, and Convergence Zones in Turbulent Flows.

[20] Kramer, Werner, H. J. H. Clercx, G. J. F. van Heijst, 2007, Vorticity dynamics of a dipole colliding with a no-slip wall. *Physics of Fluids*, Vol.19.12 pp.126603

[21] Koumoutsakos, P., 1997, Active control of vortex ?wall interactions. *Physics of Fluids* Vol 9.12 pp.3808-3816.